Analysis, quantification, and discussion of the approximations introduced by pulsed 3D-LiDARs

Stefano Cattini, *Member, IEEE*, Davide Cassanelli, Giorgio Di Loro, Luca Di Cecilia, Luca Ferrari and Luigi Rovati, *Member, IEEE,*

***Abstract*—LiDARs are considered essential for the environmental sensing required by most ADAS, including autonomous driving. Such has led to significant investments resulted in the availability of countless measuring systems that are increasingly performing and less expensive. Nevertheless, the extremely high speed of light still leads to a non-negligible quantization error in the direct time-of-flight (ToF) measure at the base of pulsed LiDARs — the leading technology for automotive applications. Hence, pulsed 3D-LiDARs analyze the surrounding by approximating and deforming it on concentric spheres whose radii are quantized with a quantization step that, for most commercial systems, is on the order of some centimeters. The deformation and error introduced by such quantization can thus be significant. In this study, we point out the approximations and assumptions intrinsic to 3D-LiDARs and propose a measurement procedure that, through the analysis of the fine variations of the target position, allows an accurate investigation of the axial resolution and error — probably among the few limitations still affecting this technology. To the best of our knowledge, this is the first study focused on the detailed analysis of the quantization error in 3D-LiDARs. The proposed method has been tested on one of the most popular 3D-LiDARs — namely the MRS 6000 by Sick. The obtained results revealed for the MRS 6000 a quantization step of about 6 cm (ToF quantization of about 0.4 ns) and an axial error normally distributed with experimental standard deviation of about 30 mm.**

***Index Terms*—LiDAR, LADAR, ToF, Terrestrial laser scanner, Measurement, Autonomous driving, ADAS.**

I. Introduction

Promoted by the strong demand for high-performing ADAS (Advanced Driver Assistance System) and the goal of autonomous driving, 3D-LiDARs have seen considerable investments that have increased their performance and, in general, significantly reduced their costs. The availability of high-performance and lower-cost LiDARs had also promoted the spread of such measuring systems to many other applications. Thus, 3D-LiDARs are nowadays finding more and more applications in fields such as industrial automation and agriculture. The high interest in LiDARs has also resulted in a considerable number of studies that have been recently published both on the design [1]–[9] and characterization [10]–[18] of LiDAR systems and subsystems.

LiDARs are generally recognized to provide better accuracy in estimating distances than other measuring systems such as radars, ultrasonic sensors and, stereo-cameras, becoming one of the pillars for autonomous vehicles [19], [20]. The increase in performance of both the LiDARs and the rendering software tends to make us forget the approximations and assumptions incorporated in the measurement principle at the basis of 3D-LiDARs and, therefore, the limits of such technology. Nonetheless, as described in more detail in section II, pulsed 3D-LiDARs — the leading technology in automotive [20] — analyze the surrounding by "sampling" it on concentric spheres whose rays differ of δd — the axial-distance quantum. LiDARs thus analyze the surrounding by approximating and deforming it on a fixed set of spheres. Flat surfaces are hence bent on spherical caps whose radii differ by δd. Given that, in the vast majority of the current commercial systems, δd is on the order of some centimeters, and that, due to the measurement error, points may differ by some quanta to the real positions, the deformation introduced by such quantization can be significant.

This article is hence aimed at pointing out the approximations and assumptions incorporated in the measurement principle at the basis of 3D-LiDARs, with particular focus on pulsed 3D-LiDARs, thus warning the user about its intrinsic limits. As described in more detail in section II, one of the main aspects is related to the axial-distance measure. Therefore, the main sources of uncertainty in the axial-distance measure obtained through the direct ToF (time-of-flight) measure are described and a measurement procedure for their quantification is proposed. Indeed, although manufacturers often report some information about the axial error, such information is usually generic and, to the best of our knowledge, no information is normally provided regarding aspects such as, for example, standard uncertainty or coverage probability. To quantify all such aspects, this study proposes a careful analysis of the axial measure in pulsed 3D-LiDARs. Other studies have been proposed on the analysis of the axial error of 3D-LiDARs e.g. [14], [16], [17], [21]. Nonetheless, to the best of our knowledge, this is the first study that proposes an accurate analysis of such an error by analyzing the effects of the quantization of the axial measure. Such has been obtained through the analysis of the variation of the distribution of point-cloud (PC) points produced by fine variations of the target position.

To provide examples of the effects of the approximations

S. Cattini and L. Rovati are both with the Department of Engineering "Enzo Ferrari" and, the Interdepartmental Centre Intermech MO.RE., University of Modena and Reggio Emilia, Via Vivarelli 10, 41125, Modena, Italy. e-mail: stefano.cattini@unimore.it

Davide Cassanelli and Giorgio Di Loro are with the Department of Engineering "Enzo Ferrari", University of Modena and Reggio Emilia, Via Vivarelli 10, 41125, Modena, Italy.

L. Di Cecilia and L. Ferrari are with CNH Industrial Italia Spa, Viale delle Nazioni, 55, 41122 Modena, Italy

intrinsic in 3D-LiDARs and of the information that can be obtained through the proposed measurement method, some example results obtained from the analysis of the MRS 6000 by Sick — one of the most popular 3D-LiDARs on the market — are reported.

In the following, section II briefly introduces the approximations and assumptions intrinsic to 3D-LiDARs, section III describes the developed measurement procedure and data analysis. Examples of the results obtained exploiting the proposed measurement procedure are reported in section IV and discussion and conclusions are reported in sections V and VI, respectively.

II. Approximations and Assumptions Intrinsic to 3D-LiDARs

In its simplest configuration, the LiDAR system provides only the estimate of the axial distance d — the range — between the measuring system and the target. Nonetheless, from such simple axial information, it is possible to obtain a 3D mapping of the surrounding environment. In fact, probably most LiDAR systems currently on the market are 3D-LiDARs. To obtain such a 3D-mapping, substantially two different techniques are employed: scanning and flash. Scanning LiDARs steer one or more collimated laser beams simultaneously emitted. The mapping of the environment thus takes place sequentially by knowing the current steering direction and measuring the relative axial distance d. On the contrary, flash LiDARs scan the surrounding theoretically in a single acquisition by measuring the axial distances produced by the reflections of a single diverging beam detected by an array of detectors which "observe" different regions of the surrounding. Hence, 3D-LiDARs only measure the range, and the position of each point of the PC is estimated knowing, or supposing, the direction — elevation and azimuth angles — from which the reflection comes. Therefore, as shown in Fig. 1, as long as the receiving optics can be reasonably approximated as point-like, both scanning and flash LiDARs analyze the surrounding space by "sampling" it on concentric spheres. Such concentric spheres sampling is thus not limited to a specific 3D-LiDARs technology, but all 3D-LiDARs in general. Hence, all 3D-LiDARs analyze the surrounding by approximating and deforming it on concentric spheres whose radii differ by a distance determined by the resolution in the axial measurement. Note that the analysis of the external environment in polar coordinates is typical of many imaging systems. Indeed, rays passing through the center of a lens does not change direction. Hence, for example, each pixel of the 2D-matrix image obtained from a fixed focal length non-telecentric camera is associated with a specific pair (φ_i, θ_i) of elevation and azimuth angles in the object space.

To estimate the range, d, several technologies are available. ToF (time-of-flight) telemeters are generally classified in pulse telemeters — direct ToF measure — and, sine-wave telemeters — indirect ToF measure. Sine-wave telemeters generally exploit Amplitude Modulated Continuous Wave (AMCW) or Frequency Modulated Continuous Wave (FMCW) [22]. Most LiDARs currently used for automotive applications are pulsed [20].

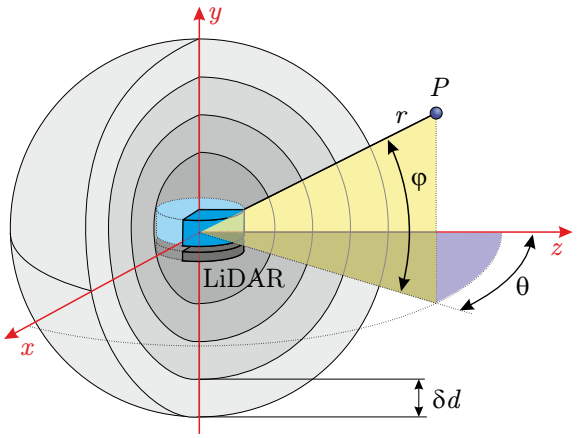

Fig. 1. Schematic representation of how 3D-LiDARs analyze the surrounding space. The radial distance, r, of every single point P composing the point-cloud is determined by the measurement of its range. The angular coordinates, (θ, φ), are determined on the basis of knowledge of the direction from which the revealed echo comes. In "scanning" LiDARs, the echo direction is supposed to coincide with the direction in which the collimated beam is currently steered. In flash-type systems, the direction is determined by the optics of the specific detector. Thus, as long as the receiving optics can be reasonably approximated as point-like, both scanning and flash technologies analyze the environment by sampling it on concentric spheres. Hence, the measure is obtained in spherical coordinates (radius r, elevation φ and azimuth θ) and usually converted to Cartesian, (x, y, z), for the creation of the point-cloud.

As the name suggests and shown in Fig. 2, pulse telemeters periodically emit pulses thus directly measuring the ToF as the time, t, the emitted pulse takes to propagate back and forth from the target. Hence, the quantization in the time measure reflects in the quantization in the distance measure:

$$\delta d = \frac{c}{n} \cdot \frac{\delta t}{2} \ , \tag{1}$$

where δt and δd are the time and distance quanta, c/n is the speed of light in the medium being c the speed of light in vacuum and n the refractive index of the propagation medium. The $1/2$ in (1) takes into account the round trip propagation. The quantization of pulsed LiDAR systems along the beam direction, sometimes referred to as the "axial-resolution", is thus primarily determined by the least significant bit of the used time-to-digital converter (TDC) [22]–[24].

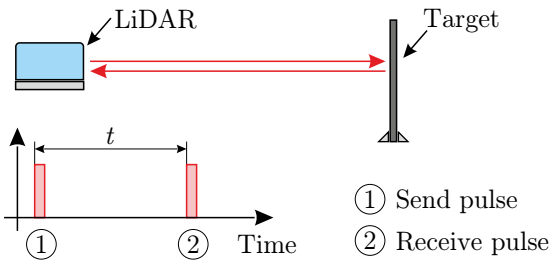

Fig. 2. Schematic representation of the direct ToF measure performed by pulse telemeters. The ToF is estimated as the time, t, the pulse takes to propagate back and forth from the measuring system to the target.

As previously introduced, regardless of the technology — scanning or flash —, as long as the receiving optics can be

reasonably approximated as point-like, each point of the point-cloud is acquired in polar coordinates:

$$P = (r, \theta, \varphi) \ , \tag{2}$$

where, as shown in Fig. 1, r is the radius and φ and, θ are the elevation and azimuth angles. Furthermore, both for scanning and flash, the analysis of the surrounding always takes place sampling on a finite and generally fixed set of directions and, therefore, on a finite and generally fixed set of elevation and azimuth angles. Since, as introduced previously, the range measure is also quantized, the values of r, θ, and φ are thus quantized. The domain (set) of allowed values can be easily determined by analyzing the PC in polar coordinates. The difference in elevation angle between adjacent points of the PC, the $\delta\varphi$ quantum, is often referred to as the "vertical angular resolution". Similarly, the difference in azimuth angle between adjacent points of the PC, the $\delta\theta$ quantum, is often referred to as the "horizontal angular resolution". Note that, while the quantization in the angles is clear and generally explicitly declared by the manufacturer, that relating to the axial measurement is normally not.

However, due to the finite resolution, also the axial distance, r, is constrained to a discrete set of values. In pulsed LiDARs, such a set has fixed values determined by the quantization step δd. In pulsed LiDARs the bins can therefore be considered as concentric spheres whose radii differ by δd along the direction of propagation of the impulse. Within a single channel — fixed elevation angle φ_i, — the points are $\delta\theta$ spaced with respect to the θ coordinate. In pulsed LiDARs the coordinates of each point of the PC are thus quantized to a fixed set and, as shown in Fig. 3, simplifying the analysis to a single channel — fixed elevation angle φ_i — the points are spaced by $\delta\theta$ along θ and lie on concentric circles whose radii differ from each other by δd — the bins.

In the flash technology — solid-state LiDARs, — the observed (φ_i, θ_i) pairs are determined by the optics and the pixels of the detector. In the scanning technology, they are determined by the system's ability to steer the beam. At present, most automotive LiDARs are scanning LiDARs and, in particular, spinning LiDARs [20] (also known as rotor-based mechanical LiDARs). The other main scanning technologies are [17], [20]: the MEMS (micro electro mechanical systems) — quasi-solid-state LiDARs — and the OPA (optical phase arrays) — solid-state LiDARs.

As the name suggests, spinning LiDARs rotate while periodically firing a laser. Therefore, the azimuth angle θ is generally estimated exploiting an encoder in closed-loop feedback control. In the past, the vertical steering of the beam was generally obtained using a moving-mirror, thus estimated exploiting a second encoder. To reduce the number of moving parts, most spinning LiDARs currently use an array of differently tilted laser diodes. The elevation angle, φ, is therefore generally determined by the inclination of the laser that generated the pulse. The number, n_φ, of φ angles is determined by the number of LiDAR channels, and each channel, CH, is therefore characterized by a specific elevation angle φ_i. On the contrary, the $\delta\theta$ is determined by the pulse emission frequency and the LiDAR angular velocity.

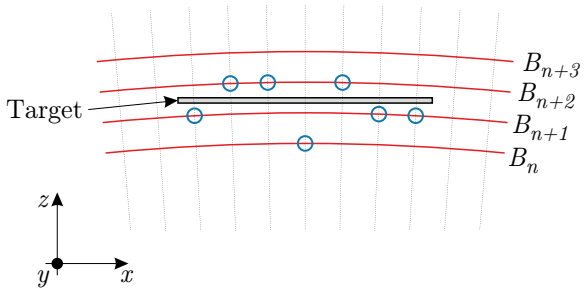

Fig. 3. Schematic representation of how a single channel — fixed elevation angle φ — of a pulsed LiDAR scans its surroundings. The "almost vertical" dashed lines (⋯) represent the beams of the pulses sequentially emitted by the LiDAR (scanning mode) or the lines of sight of the receivers composing a single channel (flash mode). The "horizontal" sections of circumferences (⌢) represent the quantization in the distance estimate. Each of such semicircles constitutes a bin, e.g. B_n, and its radius differs δd from the adjacent semicircles. The circles (○) represent the result of the sampling of the target by the LiDAR channel. Due to quantization and measurement errors, the samples (○) are distributed over several bins. (To simplify the representation the origin of the LiDAR axes has been translated to the lower-left corner of the figure).

Since the PC is acquired by the LiDAR in spherical coordinates, but transmitted by ROS (Robot Operating System) in Cartesian coordinates, in the following, both reference systems will be used, based on what will provide the simplest representation.

Note that the beams used by scanning LiDARs to sample the surrounding have a not-null cross-section [15]. Hence, if the beam spot does not hit a single flat surface but, due to its non-zero cross-section, falls on more than one object, a single pulse can give rise to multiple echoes. The same applies to the detection optics of flash LiDARs. For this reason, most LiDAR manufacturers analyze more than one echo per single emitted pulse and allow the user to choose which echo to consider for the measurement. In particular, basically all manufacturers allow the user to set the "first echo" and "last echo" modes. As the name suggests, in the "first echo" mode the distance is estimated based on the ToF of the first echo pulse received; the "last echo" mode uses the last ToF among those acquired.

III. Materials and Methods

A. Experimental set-up and measurement procedure

To investigate the axial error, we propose exploiting a setup composed of a rail and a sliding carriage as the custom one previously described [25] and shown in Fig. 4. In such a setup, the IUT (instrument under test) was fixed on a multi-axis stage (pitch and yaw platform model PY004/M by Thorlabs and XY and rotation stage model OCT-XYR1/M by Thorlabs), thus aligned to the rail exploiting the procedure described in [25]. As shown in Fig. 4, the proposed measurement setup included a planar reflective target (24" by 24" hardboard model TB4, by Thorlabs) which was fixed on the sliding carriage and thus could be translated along the rail to modify its distance, d, from the IUT. Such a distance was verified using the interferometer INT (single-axis linear interferometer model HP5527A, by HP). As shown in Fig. 4, the IUT measures the distance to the target while the INT measures the distance

to the corner cube. Furthermore, the positions of the origins of the axes of both the IUT and the INT are unknown and cannot be easily accurately determined. Hence, there is a fixed and potentially partially unknown offset between the distances estimated by the two systems even when they are correctly aligned. The method used for estimating the offset between the target distance, d, and the measure, d_{INT}, provided by the INT,

$$d_{offset} = d - d_{INT} \ , \tag{3}$$

will be described in subsection III-B.

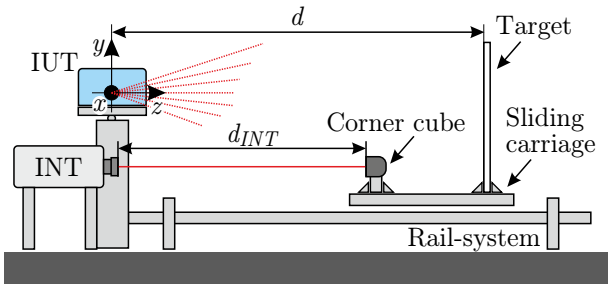

Fig. 4. Schematic representation of the measurement setup. The IUT (instrument under test) is fixed on a multi-axis stage that allows to align it to the rail-system. The dashed lines (···) represent the IUT channels (CHs). The planar reflective target is fixed on a sliding carriage that allows translating it along the rail to modify its distance, d, from the IUT. The interferometer, INT, allows to finely measure the magnitude of target translation. The system is aligned so that the target and the measurement beam of the interferometer are respectively orthogonal and parallel to the LiDAR z-axis. d is thus the distance along the z-axis between the origin of the coordinates system of the IUT and the target and, d_{INT} is the distance (along the z-axis) between the origin of the interferometer and the corner-cube (model M-BBR 1-1I by Newport).

To investigate the axial error, we thus propose to analyze the point-clouds (PCs) obtained by varying the target distance d. Such distance must be varied both in "fine" steps — steps shorter than the axial quantum δd — and in "large" steps able to highlight the various contributions of uncertainty (this aspect will be discussed in section V). The proposed method thus involves acquiring and analyzing multiple PCs for each target position. Then, to perform a statistical analysis of how the points distributed among the various bins. In the following, the proposed procedure is described in detail, also reporting the specific settings used to obtain the example results that will be shown in section IV.

After aligning IUT, INT, and target and waiting for the warm-up, the target has to be positioned at a first distance (significant for applications of interest). The results in section IV were obtained by setting $d \approx 1.4$ m.

Then, for each target position, n_{PC} PCs have to be acquired under the repeatability condition of measurement. The results in section IV were obtained setting $n_{PC} = 25$ and acquiring, for each target position, $n_{PC} = 25$ PCs both by setting the "first echo" mode and the "last echo" mode. After that, the target must be translated by a "fine" step. The length of the "fine" step determines the spatial sampling period. Since the investigated LiDAR has $\delta d = 6.25$ cm, the results in section IV were obtained using "fine" steps of 10 mm. Such a procedure has to be repeated for n_d times. n_d must be large enough to allow analyzing more bins — the fine step multiplied by n_d must be at least of the order of some δd. The results in section IV have been obtained setting $n_d = 50$ "fine" steps, thus investigating 50 cm.

As discussed in section V, by repeating the analysis also performing "large" displacements, it is possible to extract more information. As an example, the results in section IV have been obtained starting a second sampling at a distance $d \approx 6.8$ m. The average distances of approximately 1.6 m and 7 m were chosen as, on the one hand, arbitrarily considered significant for many practical applications and, on the other hand, the characteristics of the setup would have made it difficult to analyze shorter distances. Consider that the greater the target distance, the smaller the deformation of flat surfaces introduced by the sampling on the spherical surfaces and the relative error introduced by the quantization in the axial measure. Also consider that, as discussed in section V, the optical power of the pulse received when the target is at 7 m is about 1/20 compared to the optical power received when it is at 1.6 m. Therefore, such ranges also allow obtaining an estimate, albeit rough, of the effect due to a variation of the power of the received pulse (e.g. due to a different target reflectance). Obviously, the method can also be applied for the analysis of other distances of interest.

B. Axial-error analysis

The single-point axial-error was investigated by analyzing a single point P for each of the acquired PCs thus, analyzing both how such P point distributed among the various bins within the n_{PC} measures acquired under the repeatability condition of measurement and how such distribution varied as the position d of the target varied. The results in section IV were obtained analyzing the point P defined by $\varphi = \varphi_{CH}$ and $\theta = 0°$. Hence, defining $\Psi(n, d)$, $n \in [1, n_{PC}]$, as the the set of all points composing the n^{th} PC acquired at distance d, the analyzed point was:

$$P(n, d) = \Psi_{PC}(n, d) | (\varphi = \varphi_{CH}, \theta = 0°) \ , \tag{4}$$

where φ_{CH} is the elevation angle of the analyzed CH. Each point, P, was therefore defined by the value of its radius and such a value, r_P, is a discrete random variable that can only assume the values corresponding to the radii of the IUT bins — pulsed LiDAR.

The statistical analysis was performed analyzing the empirical probability density function Γ, thus analyzing the number of times that the P point fell into each bin. Defining $\Lambda(d)$ as the set of P points obtained from the n_{PC} measures acquired at the distance d, for each target distance, d, the empirical probability density function (probability mass function) was calculated as:

$$\Gamma(d, r_{bin}) = \frac{\mathbf{card}\big[\Lambda(d) | r_P = r_{bin}\big]}{\mathbf{card}\big[\Lambda(d)\big]} \ , \tag{5}$$

where $\mathbf{card}[\dots]$ is the cardinality, r_{bin} is the value of the radius of the considered bin and, $\mathbf{card}[\Lambda(d)] = n_{PC}$.

For each position d, the mean distance estimated by the IUT, $\overline{d_{IUT}}$, was calculated as

$$\begin{aligned}\overline{d_{IUT}}(d) =& \frac{1}{n_{PC}} \cdot \sum_{n=1}^{n_{PC}} r_P(n,d) \\ s_{\overline{d_{IUT}}}(d) =& \sqrt{\frac{\sum_{n=1}^{n_{PC}} \left[r_P(n,d) - \overline{d_{IUT}}(d)\right]^2}{n_{PC} \cdot (n_{PC}-1)}} \ .\end{aligned} \tag{6}$$

where $s_{\overline{d_{IUT}}}(d)$ is the respective experimental standard deviation of the mean.

The offset, d_{offset}, between the target distance, d, and the measure, d_{INT}, provided by the INT was estimated as the intercept of the linear interpolation of the sets of $\overline{d_{IUT}}(d)$ and $d_{INT}(d)$ values obtained translating the target along the rail [17]. In the interpolation, the angular coefficient was set equal to 1. The resulting d_{offset} was compatible with the rough estimate obtained using a tape measure. Note that the estimate of d_{offset} as the intercept of the linear interpolation compensates for any possible offset error of the IUT, thus preventing the possibility of detecting such error unless large enough to be evidenced by the tape measure verification.

For each target position, both the error $\epsilon(n,d)$, relative to each single PC, and the average error, $\bar{\epsilon}(d)$, relative to the n_{PC} PCs acquired under the repeatability condition of measurement, were calculated as:

$$\begin{aligned}\epsilon(n,d) =& d_{INT}(d) + d_{offset} - r_P(n,d) \\ \bar{\epsilon}(d) =& d_{INT}(d) + d_{offset} - \overline{d_{IUT}}(d) \ ,\end{aligned} \tag{7}$$

where, according to (3), $d_{INT}(d) + d_{offset}$ is the estimate of the target distance, d.

Note that, although the LiDAR acquires in spherical coordinates, communication with it occurs through ROS that transforms the PC into Cartesian coordinates. Based on the previous equations, it is convenient to carry out the data processing in spherical coordinates, thus transforming the ROS data back into spherical coordinates before proceeding with the analysis. Such a double transformation from spherical to Cartesian to spherical again can introduce truncation errors. Hence, points that fall within the same bin in spherical coordinates and should, therefore, have exactly the same value of r, may result, once reported back from Cartesian to spherical, to r values slightly different from each other. Thus, before analyzing the data, it is convenient to round the r values to reduce the number of significant digits. The same holds for the azimuth, θ, and elevation, φ, angles. The results reported in section IV were obtained by rounding the values to the fourth decimal place — round-off errors below to 10^{-4} m and 10^{-4} rad, respectively.

C. Warm-up and Stability

To proceed with the characterization of an instrument, it is necessary to know its warm-up time. Moreover, the acquisition of all the measures described in subsection III-A requires a non-negligible amount of time. Hence, before performing the measurements described in subsection III-B, it is important to investigate the warm-up and stability.

Such analysis was performed according to the procedure previously described [17]. The IUT was thus set to log a PC every minute, was turned off for at least 12 h, and then turned on starting the acquisition of the PCs for 15 h. Since the procedure described in subsection III-A analyzes only one point of the PC, also the warm-up and stability analysis analyzes only one point of the PC, that is, $P(t)$. In particular, according to subsection III-B, supposing $\Psi(t)$ to be the set of point composing the PC acquired at time t, we analyzed:

$$P(t) = \Psi_{PC}(t) | (\varphi = \varphi_{CH}, \theta = 0^\circ) \ . \tag{8}$$

As described above, P can only take a finite number of values. Therefore, the warm-up and stability analysis examined how P distributed in the various bins as time t changed and, in particular, analyzed it with movable windows having a width equal to n_{PC}. Defining $\Omega(n)$ as the set of all the P points acquired up to the n^{th} sampling instant t_n, if $P(t)$ is stationary, the expected value of the ratio

$$\Xi(n + n_{PC}/2, r_{bin}) = \frac{\mathbf{card}\left[\Omega(n+n_{PC}-1) | r_P = r_{bin}\right] - \mathbf{card}\left[\Omega(n) | r_P = r_{bin}\right]}{n_{PC}} \ , \tag{9}$$

calculated at the distance d coincides with the expected value of $\Gamma(d, r_{bin})$. That is, for each value of n — t_n — $E\left[\Xi(n, r_{bin})\right]$ calculated at d equals $E\left[\Gamma(d, r_{bin})\right]$ — $E[\dots]$ is the expected value. The warm-up and stability were thus investigated by analyzing $\Xi(n, r_{bin})$.

IV. Results

As previously introduced, to provide examples of the effects of the approximations intrinsic in pulsed 3D-LiDARs and of the information that can be obtained through the proposed measurement procedure, in this section some results obtained from the analysis of the pulsed (spinning) LiDAR model MRS 6000 by Sick — one of the most popular 3D-LiDARs — are reported. The settings of the IUT — the MRS 6000 — during the test are resumed in Table I. Tests were performed in a controlled environment where both temperature and lighting were monitored.

Fig. 5 shows two examples of PCs acquired by the IUT once the target was at $d \approx 1.43$ m and $d \approx 7.27$ m, respectively.

TABLE I
SETTINGS OF THE IUT (MRS 6000 BY SICK).

Quantity	Value
Scanning frequency f_{scan}	10 Hz
Echo analysis	"first echo" and "last echo"
Warm-up	150 min

Fig. 5(a) clearly shows how the sampling on concentric spheres performed by 3D-LiDARs to analyze the environment deforms the flat target, bending it on spherical caps. From the PCs analysis it was also possible to determine the axial quantization $\delta d = 6.25$ cm.

As previously introduced, the warm-up and stability were analyzed by analyzing how the P point distributed among the various bins as a function of time. Fig. 6 shows the $\Xi(t, r_{bin})$ obtained for $d \approx 1.5$ m and $d \approx 7$ m. As can be seen, after

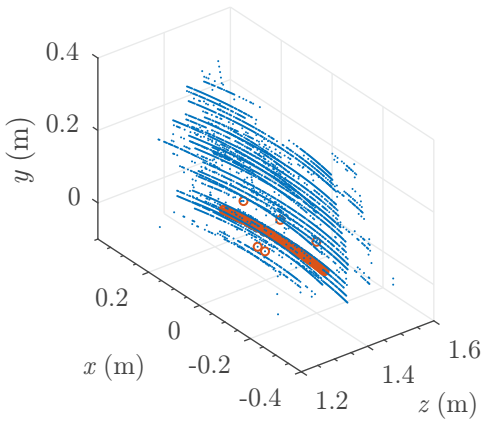

(a) $d \approx 1.43$ m, echo filter "first".

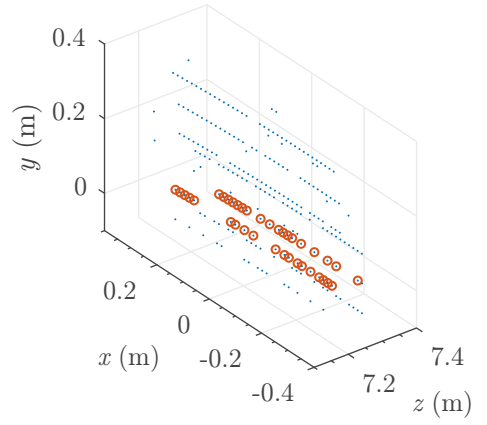

(b) $d \approx 7.27$ m, echo filter "last".

Fig. 5. Examples of point-clouds acquired by the IUT. Figure (a) shows one of the $n_{PC} = 25$ PCs acquired by the IUT once the target was at a distance $d \approx 1.43$ m (echo filter: "first"); figure (b) one of the $n_{PC} = 25$ PCs acquired at a distance $d \approx 7.27$ m (echo filter: "last"). The blue dots (•) represent all points relative to the target. The orange circles (○) represent the central points of the analyzed CH ($\varphi = \varphi_{CH}$). Depending on the position of the target with respect to the bins, the points tend to fall only on one bin (a) or to distribute themselves on adjacent bins (b).

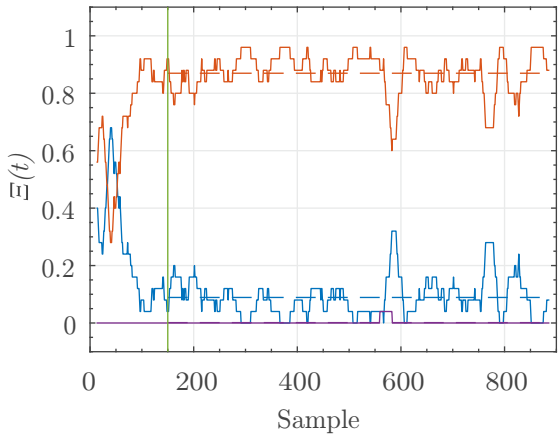

(a) $d \approx 1.5$ m, echo filter "first".

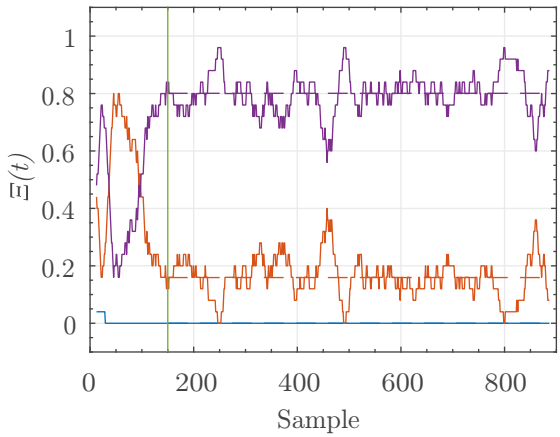

(b) $d \approx 7$ m, echo filter "last".

Fig. 6. $\Xi(t, r_{bin})$ for the three bins between which $P(t)$ distributed. The vertical lines (—) represent the warm-up time t_w. The orange, blue and, purple dashed horizontal lines (– – –) represent the mean values of $\Xi(t, r_{bin})$ calculated for $t \geq t_w$. (sampling period 1 min).

about $n = 150$ samples ($t_n = 150$ min) the trends relating to the various bins stabilize. The warm-up time, t_w was therefore set equal to 150 min. As shown in Fig. 6, within the limits of the resolution of the measurements, the drift of $\Xi(t, r_{bin})$ after t_w is negligible compared to its fluctuations.

Following the warm-up and stability analysis, the axial-error was analyzed according to the procedure described in subsection III-B.

Fig. 7 shows two examples of the distribution of the $\Lambda(d)$ points between the various bins when the target was at the distances $d \approx 1.43$ m and $d \approx 7.27$ m.

The Fig. 8 shows, for each bin, the trend of $\Gamma(d, r_{bin})$ as the target position, d, changes both for $d \in (1.3, 1.9)$ m and $d \in (6.8, 7.4)$ m.

Fig. 9 shows the trend of the parameters μ and σ of the Gaussian interpolants shown in Fig. 8. Fig. 10 shows the distribution of the errors ϵ obtained considering all the acquired measurements, that is, $n_{PC} = 25$ measures for each of the $n_D = 50$ distances. Fig. 11 shows the mean errors $\bar{\epsilon}$ obtained by finely moving the target in $d \in (1.3, 1.9)$ m and $d \in (6.8, 7.4)$ m, respectively.

V. Discussion

As introduced in section II, the axial-quantum, δd, for pulsed LiDARs based on a TDC is determined by the time quantum, δt, thus by least significant bit (LSB) of the TDC. TDC techniques and error-budget have been recently reviewed by Tancock *et al.* [26] and Rovera *et al.* [27]. In addition to the time quantization error, the main sources of the axial-error in pulsed LiDARs are noise-generated timing jitter, walk error, nonlinearity, and drift [22]–[24].

The walk error describes the effect that the amplitude and shape of the received pulse have in defining the trigger instant. The points composing $\Lambda(d)$ are relative to pulses emitted by the same laser source ($\varphi = \varphi_{CH}$) and reflected by the same target position ($\theta = 0°$), thus same reflectivity, distance d and, viewing angle. Hence, it is reasonable to suppose all the echo pulses relative to $\Lambda(d)$ to have substantially the same amplitude and shape. Therefore, regardless of the discriminator technique exploited by the TDC (e.g. edge timing, constant fraction timing, zero-crossing timing and, first-moment timing) it is reasonable to assume that all the $\Lambda(d)$ points suffer from

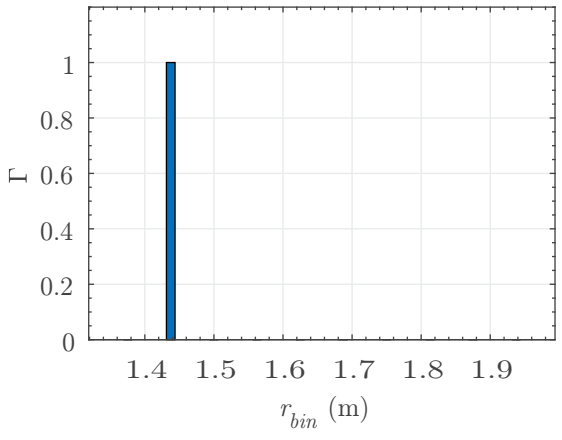

(a) $d \approx 1.43$ m, echo filter "first".

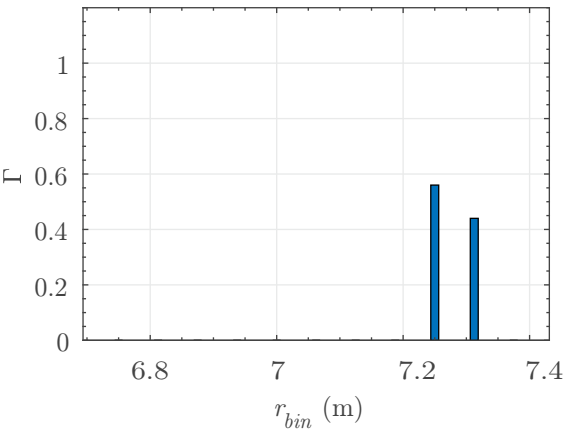

(b) $d \approx 7.27$ m, echo filter "last".

Fig. 7. Distribution of the $\Lambda(d)$ points between the various bins when the target was at distances $d \approx 1.43$ m (a) and $d \approx 7.27$ m (b). The bars represent the $\Gamma(d, r_{bin})$ values obtained from the analysis of the $n_{PC} = 25$ PCs acquired under repeatability condition of measurement. Figure (a) was obtained setting echo filter "first", whereas figure (b) was obtained setting echo filter "last".

the same walk error. Moreover, given the target displacement in steps of about 10 mm at a mean target distance of a few meters, it is also reasonable to assume the walk error to be substantially the same even for adjacent target positions, that is, for adjacent bins. On the contrary, given that the proposed measurement procedure involves analyzing two ranges having a significantly different average distance ($d \approx 1.6$ m and $d \approx 7$ m), the contribution of the walk error to the error budget should be made evident by comparing the results obtained at $d \approx 1.6$ m and $d \approx 7$ m. Indeed, consider that the power of the pulse received by the LiDAR after being reflected by the target generally reduces with the reciprocal of the square of the distance, d. Therefore, the optical power relative to the pulse received when the target is at 7 m is about 1/20 compared to the optical power received when it is at 1.6 m. Hence, it is reasonable to assume the walk error to be significantly different in the two ranges [22]–[24]. Conversely, as described in subsection III-B, since the offset, d_{offset}, between d and d_{INT} was estimated as the intercept of the linear interpolation between $\overline{d_{IUT}}(d)$ and $d_{INT}(d)$, the proposed measurement method does not allow detecting any offset error affecting the IUT unless large enough to be evidenced by the tape measure verification (that is, of the order of at least a few centimeters).

The previous considerations are generally valid as they are intrinsic to the proposed measurement procedure. More information on the specific IUT can be obtained by analyzing the experimental results reported in section IV.

As shown in Fig. 6, within the limits of the resolution of the measurements, the drift of $\Xi(t, r_{bin})$ after t_w is negligible compared to its fluctuations. Therefore, at least within the limits of the resolution obtained, the drift in 750 min is negligible.

Regarding the walk error, given that the results reported in section IV show statistically similar behavior in the two ranges ($d \approx 1.6$ m and $d \approx 7$ m), it is reasonable to assume that for the IUT the contribution of the walk error on the error budget is negligible.

Regarding quantization, according to Rovera *et al.* [27], it is expected to behave like a uniform random variable with type B uncertainty equal to $\delta_t/\sqrt{12}$. Given that the distributions shown in Figs. 8 and 10 are not uniform, but reasonably normal, it is reasonable to assume that the effect of quantization it is not the only one to consider when defining uncertainty but that noise plays an important role. The main noise sources in the analog front-end electronic of the LiDAR are the shot noise, caused by both the detected pulse and the background radiation, and, the noise generated by the electronics [24]. According to Amann *et al.* [24], the precision of the distance d measurement is thus usually mainly determined by the jitter in timing, thus proportional to root mean square amplitude of noise and inversely proportional to the slope of the timing pulse at the moment of timing.

Fig. 10 reveals for the MRS 6000 an almost normal random variable with σ of about 30 mm. Such a result clarifies and quantifies the quite generic information provided by the manufacturer — "Statistical error 30 mm" [28]. Indeed, in light of the results shown in Fig. 10, the random variable is reasonably Gaussian and, the coverage probability associated with the interval ±30 mm is about 68%. Also, note that the LiDAR performance can be significantly affected by the target reflectance. However, the results shown in Fig. 10 reveal substantially the same σ for both ranges. Since the optical power of the pulse received when the target is at 7 m is about 1/20 compared to the optical power received when it is at 1.6 m, at least within the limits of the analyzed distances, the IUT appears to be robust against variations in the reflectance of the target. That is, it is reasonable to assume that two targets that are at a distance of about 1.6 m give rise to the same σ even if their reflectances differ by 20 times.

Finally, also note that, within the limits of the precision given by the standard deviation of the Gaussian functions, the results shown in Fig. 9 indicates that the IUT is not affected by appreciable linearity errors. Furthermore, given the compatibility between the estimate of d_{offset} obtained from the linear interpolation and the tape measure (subsection III-B), even the offset error, if present, is expected to be limited — not exceeding a few centimeters.

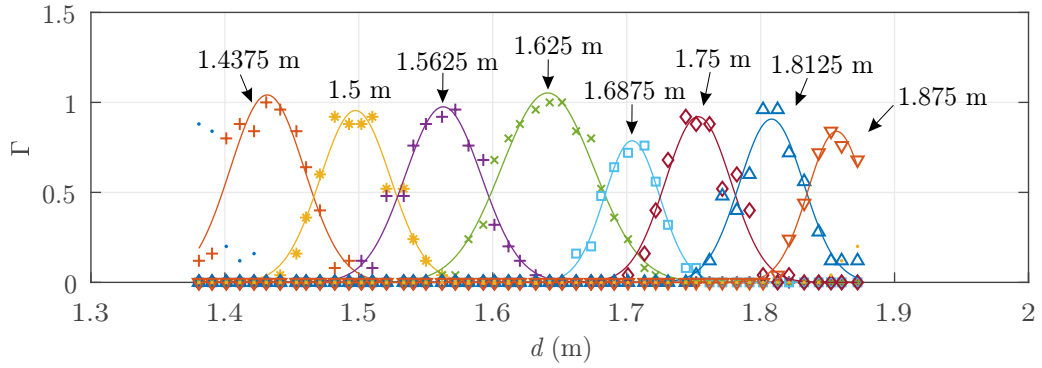

(a) $d \in (1.3, 1.9)$ m and echo filter "first".

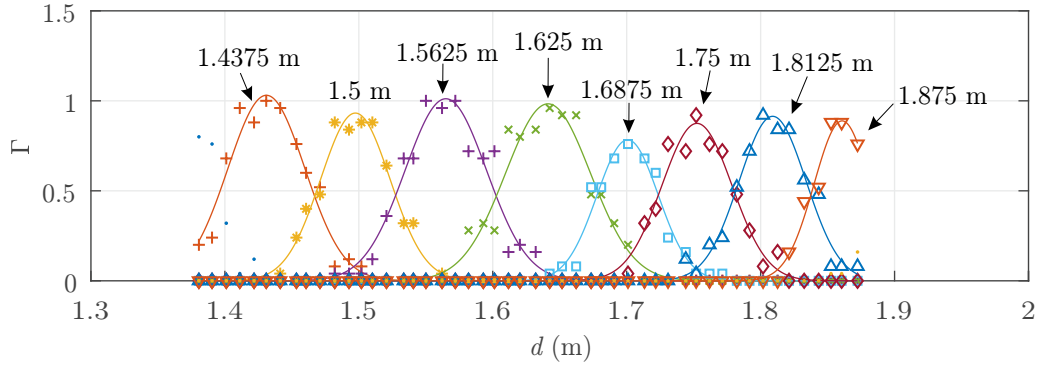

(b) $d \in (1.3, 1.9)$ m and echo filter "last".

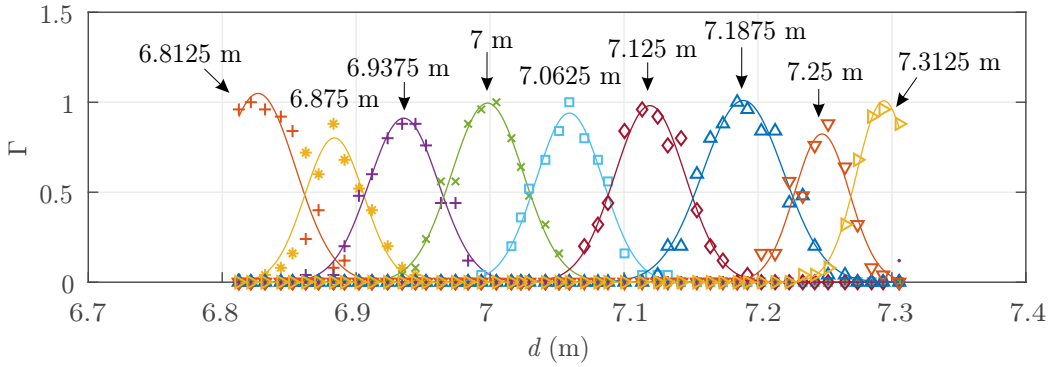

(c) $d \in (6.8, 7.4)$ m and echo filter "first".

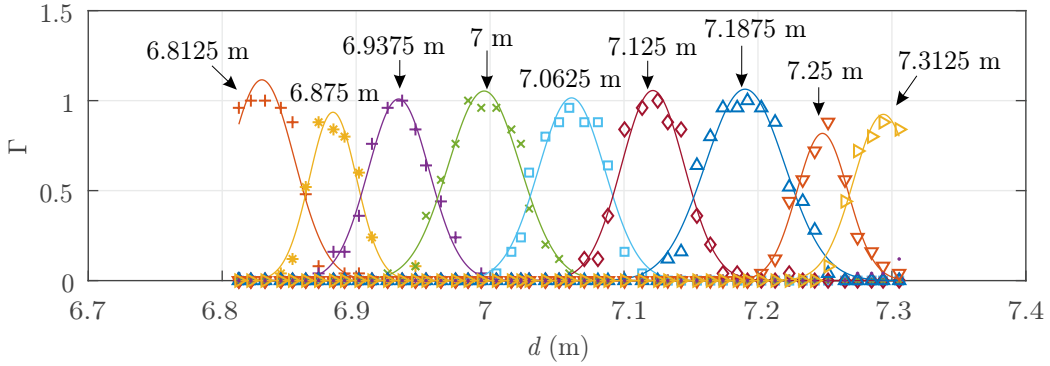

(d) $d \in (6.8, 7.4)$ m and echo filter "last".

Fig. 8. Distribution of the $\Gamma(d, r_{bin})$ as a function of target position d. Each curve (solid line) represents the Gaussian function obtained by fitting the $\Gamma(d, r_{bin})$ values relative to a specific bin; the numbers on the top of the curve represent the r_{bin} values. As an example, as shown in (a), when the target was at d = 1.502 m, almost all the $\Lambda(d)$ points fell on bin r_{bin} = 1.5 m (*) and only a few points fell in r_{bin} = 1.5625 m (+) — $\Gamma(d, r_{bin}$ = 1.5 m) = 0.88 and $\Gamma(d, r_{bin}$ = 1.5625 m) = 0.12. On the contrary, when the target was at d = 1.5206 m, the $\Lambda(d)$ points distributed among the bins r_{bin} = 1.5 m (*) and r_{bin} = 1.5625 m (+) — $\Gamma(d, r_{bin}$ = 1.5 m) = 0.52 and $\Gamma(d, r_{bin}$ = 1.5625 m) = 0.48.

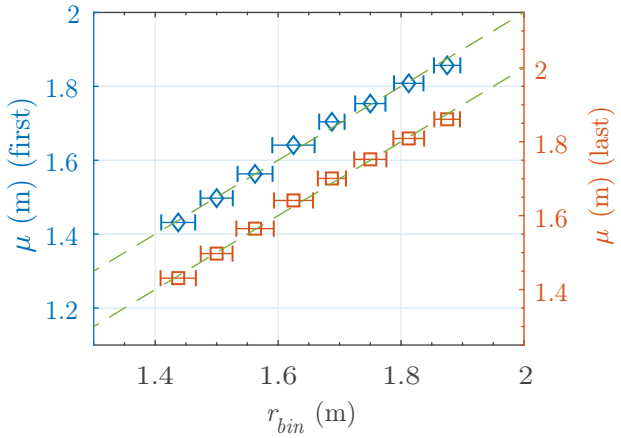

(a) $d \in (1.3, 1.9)$ m.

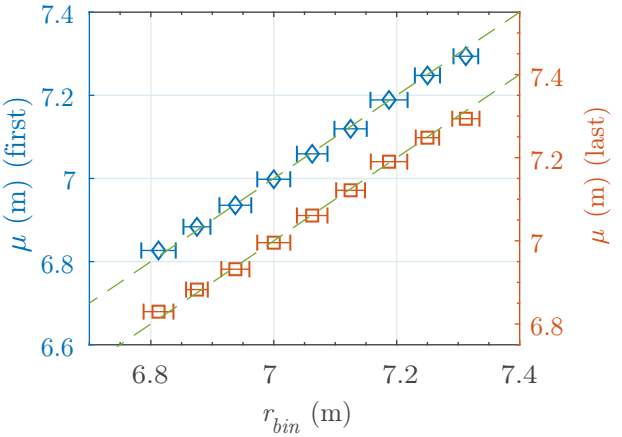

(b) $d \in (6.8, 7.4)$ m.

Fig. 9. Trend of the Gaussian interpolants as a function of the nominal value of the bins. For each bin (r_{bin}), the diamond (◇) represents the mean value μ of the Gaussian function shown in Fig. 8 obtained by setting "echo first". The square (□) represents the mean value μ of the Gaussian function obtained by setting "echo last". The errorbars represent the standard deviations σ of the Gaussian functions. The dashed lines (– –) represent the bisector of the first quadrant.

VI. Conclusions

Although LiDAR technology has benefited from significant investments which have resulted in the availability of countless measuring systems more and more performing, the quantization error in the direct time-of-flight (ToF) measure at the base of pulsed LiDARs still gives rise to quantization in the axial measure that, for most commercial systems, is on the order of some centimeters. The objective of this study is thus, on the one hand, to point out the approximations and assumptions incorporated in the measurement principle at the basis of pulsed 3D-LiDARs, and, on the other hand, to propose a measurement procedure for quantifying and analyzing the uncertainty in axial measurement.

Section II starts describing the approximations and assumptions intrinsic to all 3D-LiDARs, thus introducing as each point of the PC is acquired by the measuring system in polar coordinates and, as the analysis of the surrounding always takes place sampling on a finite and generally fixed set of directions, thus on a finite and generally fixed set of elevation and azimuth angles. Then, the analysis focus on pulsed 3D-

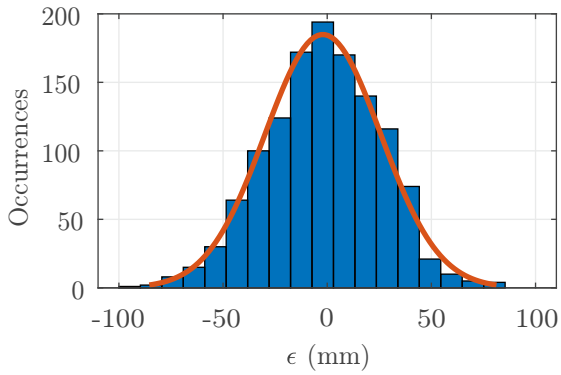

(a) $d \in (1.3, 1.9)$ m, echo "first" (values obtained from the Gaussian fitting: $\mu_\epsilon = -2.08$ mm, $\sigma_\epsilon = 27.77$ mm).

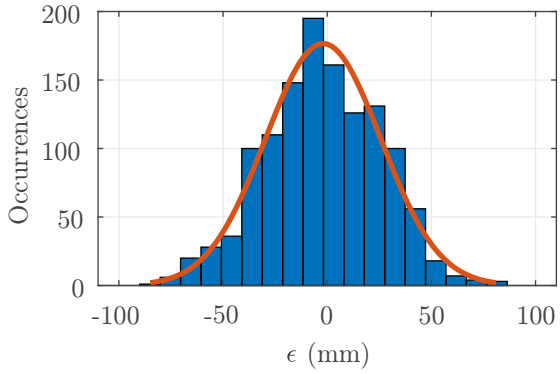

(b) $d \in (1.3, 1.9)$ m, echo "last" (values obtained from the Gaussian fitting: $\mu_\epsilon = -1.98$ mm, $\sigma_\epsilon = 27.67$ mm).

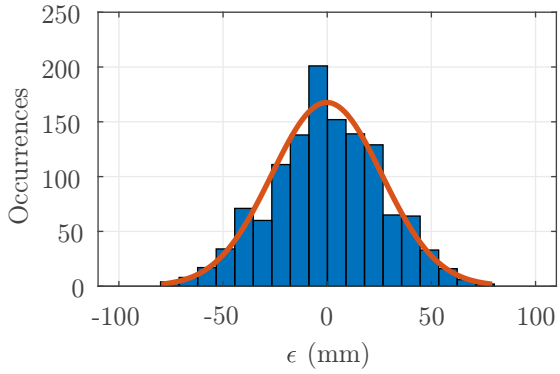

(c) $d \in (6.8, 7.4)$ m, echo "first" (values obtained from the Gaussian fitting: $\mu_\epsilon = -0.21$ mm, $\sigma_\epsilon = 26.47$ mm).

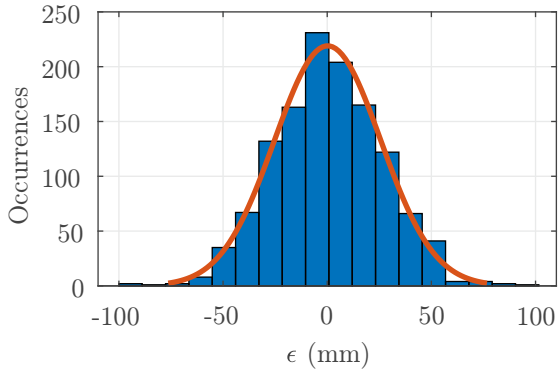

(d) $d \in (6.8, 7.4)$ m, echo "last" (values obtained from the Gaussian fitting: $\mu_\epsilon = 0.19$ mm, $\sigma_\epsilon = 25.52$ mm).

Fig. 10. Distribution of the errors ϵ. The height of each bar represents the number of errors that fell within the range defined by the base of the bar. The orange curve (—) represents the result of the fitting with a Gaussian function.

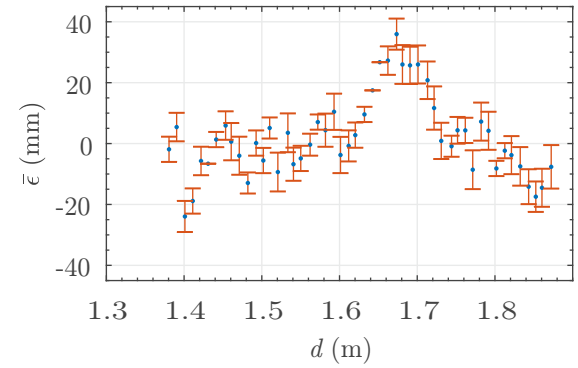

(a) $d \in (1.3, 1.9)$ m, echo "first".

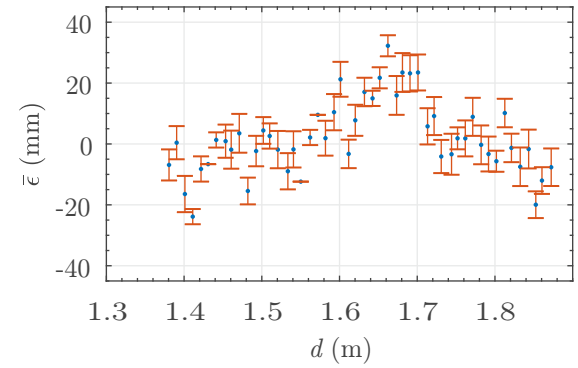

(b) $d \in (1.3, 1.9)$ m, echo "last".

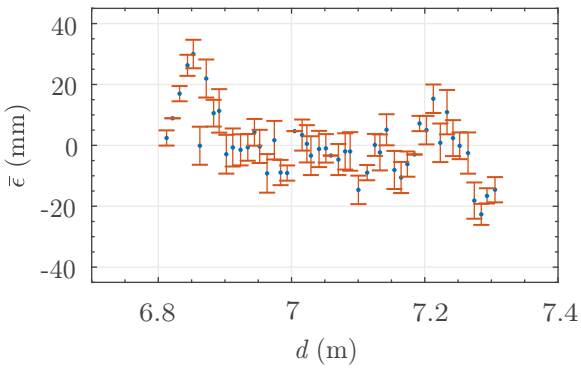

(c) $d \in (6.8, 7.4)$ m, echo "first".

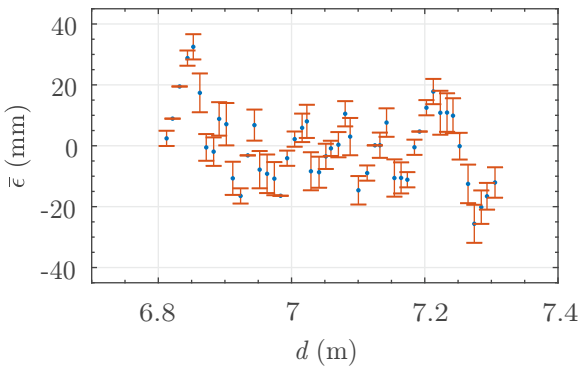

(d) $d \in (6.8, 7.4)$ m, echo "last".

Fig. 11. Mean errors $\bar{\epsilon}(\cdot)$ obtained by finely moving the target in $d \in (1.3, 1.9)$ m and $d \in (6.8, 7.4)$ m, respectively. The errorbars (1) represent the experimental standard deviations of the mean $s_{\overline{d_{IUT}}}(d)$.

LiDARs, the leading LiDAR technology in automotive, and describes as such measuring systems analyze the surrounding by approximating and deforming it on concentric spheres whose radii are quantized to a fixed set of values determined by the ToF measure.

Sections III and V describe the main sources of uncertainty in the axial-distance measure of pulsed 3D-LiDARs and propose and discuss a measurement procedure for its quantification and analysis. As previously introduced, other studies have been proposed on the analysis of the axial error of 3D-LiDARs. The novelty of this study lies in the fact that, to the best of our knowledge, for the first time, it: i) highlights and analyzes the effects related to the quantization of the axial measurement in pulsed 3D-LiDARs, ii) describes how such measuring instruments analyze the surrounding by approximating and deforming it on concentric spheres whose radii are quantized and provides a measurement procedure for measure, quantify, and, iii) analyze the uncertainty in the axial measure.

Being based on the statistical analysis of how the points of the PC are distributed among the various bins as the target position varies, the proposed procedure can be applied to any LiDAR affected by the axial quantization and, therefore, to all pulsed LiDARs and also to "non-pulsed" LiDARs that exhibit such a quantization in axial measure.

To provide examples of the effects of the approximations intrinsic in pulsed 3D-LiDARs and of the information that can be obtained through the proposed measurement method, it has been applied on one of the most popular 3D-LiDARs — namely the MRS 6000 by Sick. The results reported in section IV revealed a quantization step of about 6 cm (ToF quantization of about 0.4 ns) and an axial error normally distributed with an experimental standard deviation of about 30 mm. From the obtained data, it was also possible to determine that, within the limits of the resolution of the measurements, the drift after $t_w = 150$ min is negligible. Furthermore, at least for the analyzed distances, also the contribution of the walk error, as well as non-linearity are negligible. Moreover, given the normal distribution, it was also possible to deduce that for the MRS 6000 the uncertainty in the axial measure is not dominated by the quantization in the ToF measure but that noise, reasonably mainly the jitter in timing, plays an important role.

References

[1] F. Wang, Y. Zhuang, H. Gu, and H. Hu, "Automatic generation of synthetic LiDAR point clouds for 3-d data analysis," *IEEE Transactions on Instrumentation and Measurement*, vol. 68, no. 7, pp. 2671–2673, July 2019.

[2] S. Xie, D. Yang, K. Jiang, and Y. Zhong, "Pixels and 3-D points alignment method for the fusion of camera and LiDAR data," *IEEE Transactions on Instrumentation and Measurement*, vol. 68, no. 10, pp. 3661–3676, 2019.

[3] R. Ma, M. Liu, H. Zheng, R. Ma, and Z. Zhu, "A 66db linear dynamic range, 100 dBΩ transimpedance gain TIA with High Speed PDSH for LiDAR," *IEEE Transactions on Instrumentation and Measurement*, 2019.

[4] S. Saponara and B. Neri, "Radar sensor signal acquisition and multi-dimensional FFT processing for surveillance applications in transport systems," *IEEE Transactions on Instrumentation and Measurement*, vol. 66, no. 4, pp. 604–615, April 2017.

[5] B. Fu, Y. Wang, X. Ding, Y. Jiao, L. Tang, and R. Xiong, "LiDAR-Camera Calibration under Arbitrary Configurations: Observability and Methods," *IEEE Transactions on Instrumentation and Measurement*, 2019.

[6] S. Kurtti, J. Jansson, and J. Kostamovaara, "A CMOS Receiver-TDC Chip Set for Accurate Pulsed TOF Laser Ranging," *IEEE Transactions on Instrumentation and Measurement*, 2019.

[7] C. Ma, Y. Guo, Y. Lei, and W. An, "Binary volumetric convolutional neural networks for 3-d object recognition," *IEEE Transactions on Instrumentation and Measurement*, vol. 68, no. 1, pp. 38–48, Jan 2019.

[8] A. Hejazi, S. Oh, M. R. U. Rehman, R. E. Rad, S. Kim, J. Lee, Y. Pu, K. C. Hwang, Y. Yang, and K.-Y. Lee, "A low-power multichannel time-to-digital converter using all-digital nested delay-locked loops with 50-ps resolution and high throughput for LiDAR sensors," *IEEE Transactions on Instrumentation and Measurement*, vol. 69, no. 11, pp. 9262–9271, 2020.

[9] D. Li, M. Liu, R. Ma, and Z. Zhu, "An 8-ch LiDAR receiver based on TDC with multi-interval detection and real-time $in\ situ$ calibration," *IEEE Transactions on Instrumentation and Measurement*, vol. 69, no. 7, pp. 5081–5090, 2020.

[10] M. A. Cooper, J. F. Raquet, and R. Patton, "Range information characterization of the hokuyo UST-20LX LIDAR sensor," *Photonics*, vol. 5, no. 2, 2018. [Online]. Available: https://www.mdpi.com/2304-6732/5/2/12

[11] Z. Wang, Y. Liu, Q. Liao, H. Ye, M. Liu, and L. Wang, "Characterization of a RS-LiDAR for 3D perception," in *2018 IEEE 8th Annual International Conference on CYBER Technology in Automation, Control, and Intelligent Systems (CYBER)*, July 2018, pp. 564–569.

[12] P. K. Rachakonda, B. Muralikrishnan, M. Shilling, D. Sawyer, and G. Cheok, "An overview of activities at NIST towards the proposed ASTM E57 3D imaging system point-to-point distance standard," *Journal of the CMSC*, vol. 12, no. 2, pp. 1–14, 2017.

[13] A. G. Kashani, M. J. Olsen, C. E. Parrish, and N. Wilson, "A Review of LIDAR Radiometric Processing: From Ad Hoc Intensity Correction to Rigorous Radiometric Calibration," *Sensors*, vol. 15, no. 11, pp. 28 099–28 128, 2015. [Online]. Available: http://www.mdpi.com/1424-8220/15/11/28099

[14] J. Laconte, S. Deschenes, M. Labussiere, and F. Pomerleau, "Lidar measurement bias estimation via return waveform modelling in a context of 3D mapping," in *2019 International Conference on Robotics and Automation (ICRA)*, 2019, pp. 8100–8106.

[15] S. Cattini, L. Di Cecilia, L. Ferrari, and L. Rovati, "Optical characterization of the beams generated by 3D-LiDARs: proposed procedure and preliminary results on MRS1000," *IEEE Transactions on Instrumentation and Measurement*, vol. 69, no. 10, pp. 7796–7804, 2020. [Online]. Available: https://doi.org/10.1109/TIM.2020.2984137

[16] J. Lambert, A. Carballo, A. M. Cano, P. Narksri, D. Wong, E. Takeuchi, and K. Takeda, "Performance analysis of 10 models of 3D LiDARs for automated driving," *IEEE Access*, vol. 8, pp. 131 699–131 722, 2020.

[17] S. Cattini, D. Cassanelli, L. D. Cecilia, L. Ferrari, and L. Rovati, "A procedure for the characterization and comparison of 3-D LiDAR systems," *IEEE Transactions on Instrumentation and Measurement*, vol. 70, pp. 1–10, 2021.

[18] A. Eshkoli and Y. Nemirovsky, "Characterization and architecture of monolithic N^+P-CMOS-SiPM array for ToF measurements," *IEEE Transactions on Instrumentation and Measurement*, vol. 70, pp. 1–9, 2021.

[19] R. Thakur, "Scanning LIDAR in advanced driver assistance systems and beyond: Building a road map for next-generation LIDAR technology," *IEEE Consumer Electronics Magazine*, vol. 5, no. 3, pp. 48–54, July 2016.

[20] R. Roriz, J. Cabral, and T. Gomes, "Automotive LiDAR Technology: A Survey," *IEEE Transactions on Intelligent Transportation Systems*, pp. 1–16, 2021, early Access, 10.1109/TITS.2021.3086804.

[21] M. Tsakiri, V. Pagounis, and O. Arabatzi, "Evaluation of a pulsed terrestrial laser scanner based on ISO standards," *Surface Topography: Metrology and Properties*, vol. 3, no. 1, p. 015006, feb 2015. [Online]. Available: https://doi.org/10.1088%2F2051-672x%2F3%2F1%2F015006

[22] S. Donati, *Electro-Optical Instrumentation: Sensing and Measuring with Lasers*. Prentice Hall, 2004.

[23] T. Bosch and M. Lescure, Eds., *Selected Papers on Laser Distance Measurement*, ser. SPIE Milestone. SPIE Optical Engineering Press, 1995, vol. MS 115.

[24] M.-C. Amann, T. M. Bosch, M. Lescure, R. A. Myllylae, and M. Rioux, "Laser ranging: a critical review of unusual techniques for distance measurement," *Optical Engineering*, vol. 40, no. 1, pp. 10 – 19, 2001. [Online]. Available: https://doi.org/10.1117/1.1330700

[25] S. Cattini, L. Rovati, L. Di Cecilia, and L. Ferrari, "Comparison of the VLP-16 LiDAR system with an absolute interferometer," in *2020 IEEE International Instrumentation and Measurement Technology Conference (I2MTC)*, 2020, pp. 1–6.

[26] S. Tancock, E. Arabul, and N. Dahnoun, "A review of new time-to-digital conversion techniques," *IEEE Transactions on Instrumentation and Measurement*, vol. 68, no. 10, pp. 3406–3417, 2019.

[27] G. D. Rovera, M. Siccardi, S. Romisch, and M. Abgrall, "Time delay measurements: estimation of the error budget," *Metrologia*, vol. 56, no. 3, p. 035004, may 2019. [Online]. Available: https://doi.org/10.1088/1681-7575/ab14bb

[28] *MRS6000 3D LiDAR sensor*, SICK AG., Erwin-Sick-Str. 1, 79183 Waldkirch, Germany, document version: 8022069/114M/2019-07-17.